4D imaging of a near-terminus glacier collapse feature through high-density GPR acquisitions

Bastien Ruols[1], Johanna Klahold[1], Daniel Farinotti[2,3], James Irving[1]

[1]Institute of Earth Sciences, University of Lausanne, Lausanne, Switzerland
5 [2]Laboratory of Hydraulics, Hydrology and Glaciology (VAW), ETH Zürich, Zürich, Switzerland
[3]Swiss Federal Institute for Forest, Snow and Landscape Research (WSL), Sion, Switzerland

Correspondence to: Bastien Ruols (bastien.ruols@gmail.com)

Abstract. Recent advancements in drone technology have introduced new possibilities for high-density 3D and 4D ground-
10 penetrating radar (GPR) data acquisition over alpine glaciers. In this study, we present a 4D dataset acquired over a near-terminus collapse feature at the Rhône Glacier in Switzerland. The survey covers an area of approximately 100 m x 150 m, consists of over 100 parallel GPR lines with a lateral spacing of 1 m, and was repeated four times between July and October 2022. The glacier's rough surface made such high-resolution and high-density surveying impossible with conventional acquisition methods, highlighting the advantages of the drone-based GPR system. The GPR data provide insights into the
15 formation of the collapse feature as well as the evolution of associated glaciological structures. Our analysis suggests that the collapse initiated where the main subglacial water channel meanders and merges with a smaller secondary channel, coinciding with a small step in bedrock topography. After initiation, the subglacial cavity expanded through a combination of ice melting and mechanical failure, with ice lamellas detaching from the cavity roof. This process led to a progressive thinning of the roof, contributing to further instability. At the surface, these subsurface processes manifested as concentric
20 circular crevasses, ultimately culminating in the collapse of the cavity roof. The GPR measurements also reveal the rapid temporal evolution of the main subglacial channel downstream of the cavity. During the observed summer, the channel underwent significant changes in both shape and size, which we attribute to the advection of warm air from the glacier's large portal and the resulting increase in melt at the channel walls.

25 **Short summary.** We demonstrate the use of a drone-based ground-penetrating radar (GPR) system to gather high-resolution, high-density 4D data over a near-terminus glacier collapse feature. We monitor the growth of an air cavity and the evolution of the subglacial drainage system, providing new insights into the dynamics of collapse events. This work highlights potential future applications of drone-based GPR for monitoring glaciers, in particular in regions which are inaccessible with surface-based methods.

30

1 Introduction

Ground-Penetrating Radar (GPR) has been a standard geophysical tool in the field of glaciology for over fifty years, enabling the detailed exploration of ice and bed structures across all types of glaciated terrain (e.g., Woodward and Burke, 2007; Schroeder et al., 2020; Schroeder, 2022). Whereas traditional GPR acquisitions consist of collecting so-called "2D

35 data" along one or a small number of profile lines, 3D GPR surveying involves the collection of data along multiple parallel lines, and is becoming increasingly common as it offers a more comprehensive view of the subsurface. 3D GPR surveys have been carried out using both helicopter-based systems (e.g., Rutishauser et al., 2016; Langhammer et al., 2018; Grab et al., 2021) and ground-based methods (e.g., Saintenoy et al., 2011; Del Gobbo et al., 2016, Egli et al., 2021a), and have the potential to provide precise estimates of ice thickness, glacier volume, and bedrock morphology (e.g., Binder et al., 2009;

40 Saintenoy et al., 2013; Langhammer et al., 2019), as well as help to map englacial and subglacial channels (e.g., Church et al., 2019, 2021; Egli et al., 2021a). As the field of 3D GPR advances, two key directions have emerged: (i) increasing the spatial density of the data, and (ii) developing 4D GPR techniques, i.e. repeating the same 3D surveys over time. High-density 3D GPR surveying involves reducing the spacing between the parallel survey lines, typically to a value on the order of the wavelength of the dominant GPR antenna frequency, to avoid spatial aliasing artifacts in the across-line direction. This

45 enhances spatial resolution and can reveal intricate details of bed structure and englacial and subglacial hydrology (e.g., Murray and Booth, 2010; Reinardy et al., 2019; Church et al., 2021). Meanwhile, 4D GPR allows capturing the temporal evolution of englacial and subglacial properties, leading for instance to the investigation of changes in their internal thermal state and hydrological system (Irvine-Fynn et al., 2006; Church et al., 2020). Despite their potential, both high-density 3D and 4D GPR surveys are labor-intensive, especially when conducted from the ground. This limits their widespread use.

50 Airborne surveys via helicopter, in contrast, are costly, environmentally impactful, and do not allow for data acquisition along closely spaced parallel profile lines. To make high-density 3D and 4D GPR surveying more feasible, innovative acquisition methods are needed.

Recent advances in drone technology have opened new and exciting GPR acquisition possibilities (Catapano et al., 2022). In cryospheric research, drone-based GPR surveys began with the use of small, lightweight, ultra-wideband (>1 GHz)

55 systems for shallow (< 1 m) snow depth and snow hydrology investigations (e.g., Jenssen et al., 2020; Tan et al., 2021; Valence et al., 2022). Most recently, Ruols et al. (2023) presented the development and detailed testing of a drone-based GPR instrument operating at a frequency of 80 MHz, specifically designed for high-density 3D surveying over alpine glaciers to depths of over 100 m. The work included presentation of a large high-density 3D GPR dataset consisting of 462 parallel profiles spaced by 1 m, totaling over 112 km of data, and covering an area of approximately 350 m x 500 m. In

60 addition, precise drone positioning using Real Time Kinematic (RTK) technology permits the accurate repetition of flight trajectories, thereby making high-density 4D data acquisitions possible.

In this paper, we present a high-density, high-resolution 4D GPR dataset acquired over a surface collapse feature on the Rhône glacier, Swiss Alps. The feature developed near the glacier's front in late 2021, evolving over an approximately

one-year period before eventually fully collapsing in early 2023. A small number of scientific publications have focused on snout-marginal surface collapses, with a few events reported in the European Alps (Stocker-Waldhuber et al., 2017; Kellerer-Pirklbauer and Kulmer, 2019), northern Europe (Lindström, 1993; Dewald et al., 2021), and North-America (e.g., Konrad, 1998; Bartholomaus et al., 2011; Dewald et al., 2021). Compiling information from 22 Swiss glaciers, Egli et al. (2021b) deduced that the frequency of such collapse events has increased since the early 2000s, likely driven by ice thinning and reductions in glacier ice flux. Focusing on one of these events from the Otemma glacier in southwestern Switzerland, they hypothesized that formation begins with a meandering subglacial channel that leads to the physical removal of ice via fluvial processes. A large air cavity further builds above the unpressurized subglacial channel, either by mechanical failure from ice lamellas or by subglacial melt due to warm air entering from the water outlet at the glacier front (Egli et al., 2021b, Räss et al., 2023). This ultimately leads to the formation of circular crevasses at the surface due to ice creep and ice roof instability, which have been later confirmed by Hösli et al. (2022) and Ogier et al. (2022).

Between July and October 2022, we conducted four drone-based 3D GPR surveys over the evolving collapse feature on the Rhône glacier, using the system described in Ruols et al. (2023). Our main objective was to monitor the temporal evolution of the air cavity beneath the circular crevasses that formed at the glacier surface and of the associated subglacial channels. Due to the size of the crevasses and the quantity of data required, such an acquisition would not have been possible with classical ground-based techniques, highlighting the new opportunities provided by drone GPR acquisitions.

First, we present the field site and GPR data, followed by a detailed description of the processing workflow used to convert the raw measurements into analyzable subsurface volumes. Next, we use the data to investigate the position, size, and temporal changes in both the air cavity and the subglacial channels. Finally, we discuss these results in the context of the formation and evolution of glacier collapse features.

2. High-density 4D GPR data acquisitions

2.1. Field site

The Rhône glacier, located in central Switzerland (Fig. 1a), serves as a significant point of interest for glaciological research thanks to its accessibility and historical documentation, with geodetic measurements dating back to the mid-19th century (GLAMOS, 2022). Having a surface area of approximately 15.1 km^2 in 2021 (GLAMOS, 2022), it is the sixth largest glacier in the Swiss Alps, even if it has experienced notable retreat in recent years (e.g., Farinotti et al., 2009; GLAMOS, 2017; GLAMOS, 2022). The glacier flows southwards from ~3600 to ~2200 m above mean sea level (a.m.s.l.), where it terminates in a recently formed proglacial lake (Tsutaki et al., 2013; Church et al., 2018). The lower ablation zone of the glacier was previously investigated using GPR by Church et al. (2019, 2020, 2021) to characterize and monitor the englacial and subglacial drainage network. In October of 2021, large circular crevasses began to form close to the tongue of the glacier, indicating the initiation of the collapse of an underground cavity (Ogier et al., 2022, Hösli et al., 2022). These crevasses continued to develop throughout the year 2022 and until total collapse occurred in early 2023 (Fig. 1b-e).
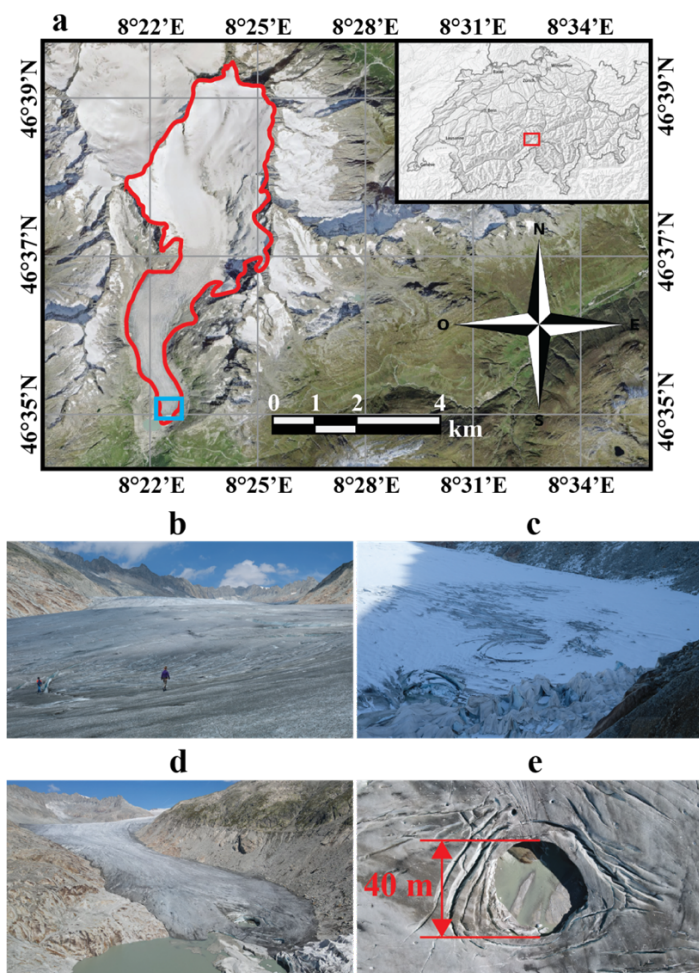
Figure 1: Geographic localization and pictures of the field site. (a) Location of the Rhône glacier (red outline) in central Switzerland (inset). The blue square indicates the region of our GPR surveys, shown in detail in Fig. 2. Inset image and satellite background from the Swiss Federal Office of Topography (Swisstopo, 2024). (b) 28 July 2022 – collapse feature in an early stage, with a clear depression in surface elevation already visible. (c) 4 October 2022 – view of the feature from further away, at a later stage of evolution and covered by snow. (d) 11 September 2023 – view of the terminal lobe of the Rhône glacier, where the feature has now fully collapsed. (e) 11 September 2023 – nadir drone photograph of the collapsed region.

100

2.2 Data acquisitions

Over the summer of 2022, we visited the tongue of the Rhône glacier four times to acquire high-density, high-resolution, 3D GPR data over the evolving collapse feature – once per month between July and October. The datasets were collected using the recently developed drone-based GPR system of Ruols et al. (2023). The system comprises the following components: (i) a DJI M300 RTK drone working with a differential GPS base station manufactured by Shenzhen DJI Sciences and Technologies (China); (ii) a custom-designed GPR controller from Utsi Electronics Ltd (UK); (iii) a True Terrain Following navigation system developed by SPH Engineering (Latvia); and (iv) a self-developed, featherweight, ~80-MHz center-frequency, single transmit-receive, resistively loaded dipole antenna. The survey trajectories were planned with the Universal ground Control Software (UgCS), with a survey line spacing of 1 m, a target altitude above the glacier surface of 5 m, and a flight speed of 4 m s^{-1} (Ruols et al., 2023). To promote the most coherent reflections from the ice-bedrock interface (Langhammer et al., 2017, 2018), survey lines were conducted across the glacier perpendicular to ice flow, with the GPR antenna oriented perpendicular to the survey line direction, as done in Ruols et al. (2023). Figures 2a-d show the raw trajectories of the four drone-based GPR acquisitions, and the specifications of each dataset are summarized in Table 1. The same programmed trajectories were flown for each acquisition, with a high level of repeatability for the horizontal positioning (Fig. 2e). However, differences in vertical positioning between acquisitions were present due to glacier melting (Fig. 2f). A picture of the GPR system acquiring data above the collapse feature is shown in Fig. 3. Advantages of a drone-based GPR acquisition are clear, as high-density data could not have been acquired on the glacier surface because of the large crevasses. Two videos from the acquisition on 4 October 2022 are provided as supplementary material: Video V1 shows the drone-based GPR system taking off and beginning the data acquisition, whereas Video V2 shows the system acquiring data over the circular crevasses.
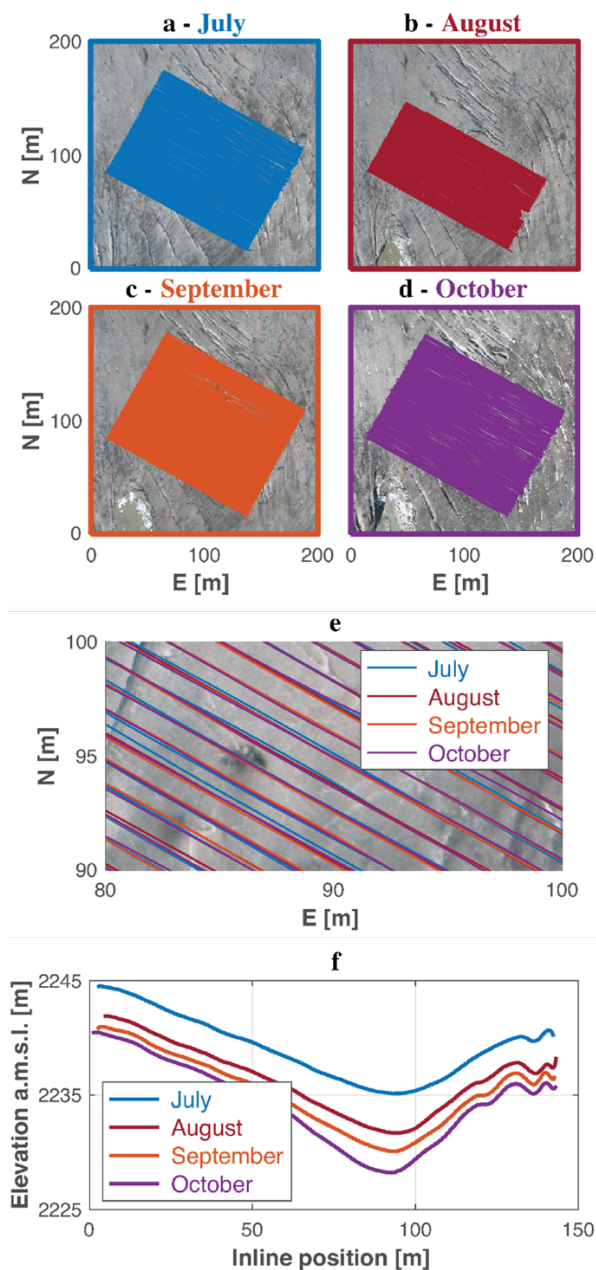
Figure 2: Survey lines flown in the four GPR acquisitions during summer 2022. (a) to (d): Flight trajectories for the July, August, September and October GPR acquisitions, respectively, plotted over the digital orthophotos (DOP) from the same month. The DOP were data acquired by photogrammetry by ETH Zürich's VAW Glaciology group. Northing (N) and Easting (E) are relative to 1159540 m and 2672690 m in the CH1903+ coordinate system, respectively. (e) Zoomed view of survey lines from the different acquisitions, superimposed on the same image. Note the high horizontal positioning repeatability of the drone GPR system. (f) Elevation a.m.s.l. of the drone-based GPR system along an example profile for the four acquisitions. The tracks differ in absolute elevation since the drone system is set to follow a given height above the glacier surface, which changes in time due to surface melt.

Table 1: GPR and photogrammetry data specifications. Note that the August GPR dataset contains less profiles than the others because the drone batteries were charged to only ~66% of their total capacity. The photogrammetry data were acquired by ETH Zürich's VAW Glaciology group.

	GPR		Photogrammetry
Date	Number of profiles	Line-km of GPR data [km]	Date
28 July 2022	104	14.78	28 July 2022
25 August 2022	71	10.02	24 August 2022
8 September 2022	108	15.33	9 September 2022
4 October 2022	107	15.32	7 October 2022
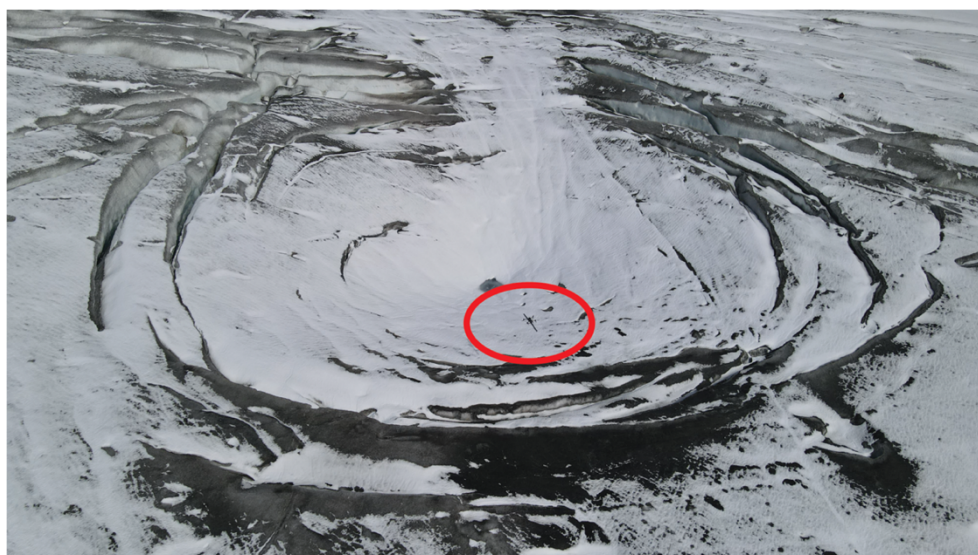
Figure 3: The drone-based GPR system (red ellipse) acquiring data over the Rhône collapse feature on 4 October 2022.

3. Data processing workflow

Our data processing workflow transforms the acquired raw GPR measurements into a 3D reflection data volume imaged in depth.

3.1 Data synchronization

In the field, two independent datasets are collected per flight: the navigation data from the drone and True Terrain Following system, and the raw GPR data from the GPR controller. The navigation data contain the information about the drone behavior, such as the flight speed, flight angles (yaw, roll, pitch), height above the ground, and precise GPS coordinates. The raw GPR data contain all of the GPR traces, tagged with GPS time. In this first step, these two independent datasets are synchronized using common GPS time, with the end result being that each GPR trace is associated with the corresponding navigational information (Ruols et al., 2023). The data from all flights conducted during a single survey are then merged to create one file per acquisition.

3.2 Binning

Next, the data from a given acquisition are segmented into individual profiles. When doing so, the positioning of each trace is corrected to take into account the distance between the GPS and GPR antennas along with the yaw, pitch, and roll angles of the drone. The latter procedure follows Ruols et al. (2023) and allows recovery of the true position of each GPR measurement. Once this is done, binning is performed to distribute the traces onto an even grid. To this end, the data positions are (i) rotated and translated to a local inline/crossline coordinate system, (ii) projected onto regularly spaced straight lines along the crossline direction having a lateral spacing of 1 m, and (iii) placed into regularly spaced bins of size 0.4 m along the inline direction. Note that each bin is filled with the closest GPR trace and that additional nearby traces are deleted, which Ruols et al. (2023) found to produce the highest quality GPR sections compared to the trace averaging. The mean distance between the center location of each bin and the true horizontal position of the GPR trace populating that bin was found to be 0.14 m.

3.3 Creation of 3D data volumes

After binning, the GPR profiles from a particular acquisition are stacked side-by-side to create a 3D GPR data volume. Because the drone-based system attempts to follow the glacier surface topography while acquiring data, vertical jumps in the recording altitude can occur between adjacent traces in the crossline direction (Ruols et al. 2023). To improve the horizontal continuity of reflection and diffraction events in the raw data volume, a static adjustment is carried out for each trace via Fourier phase shift, such that the vertical recording positions conform to a smooth acquisition surface resulting from local linear regression. Doing so was found to improve the results of migration, which is discussed in Section 3.4. Further, following previous studies involving high-density 3D GPR data (e.g., Egli et al., 2021a; Ruols et al., 2023), a relative

adjustment of the position of odd- versus even-numbered profiles is applied to reduce the so-called acquisition footprint effect. Specifically, because of small internal timing delays specific to our GPR controller and variations in the drone flight speed, a small lateral positioning adjustment between adjacent flight lines is required for best results, despite trace locations being measured with differential GPS (Ruols et al., 2023). In this regard, a constrained cross-correlation-based algorithm to determine the profile shift that maximizes the similarity between adjacent GPR profiles is applied. The results of this procedure are shown in Fig. 4 for a selected timeslice from the July 2022 dataset. After this step, the data are densified in the crossline direction using 3D linear interpolation to double the number of parallel profiles. This reduces the directional sampling bias in the original dataset and helps to mitigate migration artifacts. The final regular grid of GPR measurements has an inline spacing of 0.4 m (from the previous binning) and a crossline spacing of 0.5 m (after interpolation). Basic GPR processing is then carried out for all data volumes, which includes: (i) mean-trace removal using a 30-trace sliding window, (ii) de-wow using a 13-point residual median filter, (iii) densification of the data in time using Fourier transform interpolation, and (iv) time-zero correction. Further information about these GPR processing steps can be found in Ruols et al. (2023).

3.4 3D migration

To collapse diffraction hyperboloids in the data and to properly position reflections to their true locations in depth, we follow Egli et al. (2021a) and apply 3D topographic Kirchhoff time migration using the algorithm developed by Allroggen et al. (2014). A two-layer migration velocity model was considered, consisting of (i) an upper air layer with velocity 0.3 m ns^{-1}, the air layer thickness being calculated from the drone altimeter data (~2 cm precision), and (ii) a lower ice layer with velocity 0.167 m ns^{-1}. Considering a constant velocity for glacier ice is a standard procedure for both ground-based and airborne GPR surveys (e.g., Langhammer et al., 2017; Grab et al., 2021; Church et al., 2020), even if the effects of internal heterogeneities like water- or air-filled features are thereby neglected. This simplification causes some errors in the localization of internal features, as well as for the underlying bedrock interface, which will naturally exhibit slight variations from one acquisition to another. A migration aperture of 40 m was found to produce the most satisfactory results and is consistent with the maximum width of diffraction hyperboloids observed in the datasets. After migration, the vertical time axis is converted to depth using the assumed velocity model, which yields the final GPR data volume in space.

Figures 5a-c show part of the inline profile at a crossline position of 76 m for the July 2022 acquisition, plotted in time before migration, in time after migration, and in elevation a.m.s.l. after migration, respectively. The profile shows three main features: (i) a continuous bedrock reflection, (ii) a feature that we interpret as the roof of the subglacial cavity, and (iii) another feature that we interpret to be a multiple bedrock reflection from within the cavity. The interpretation of the cavity roof is supported by reflections in the neighboring profiles, which show a consistent pattern. Figure 6 displays the migrated and depth-converted data visualized in 3D through three selected inline profiles, crossline profiles, and timeslices.
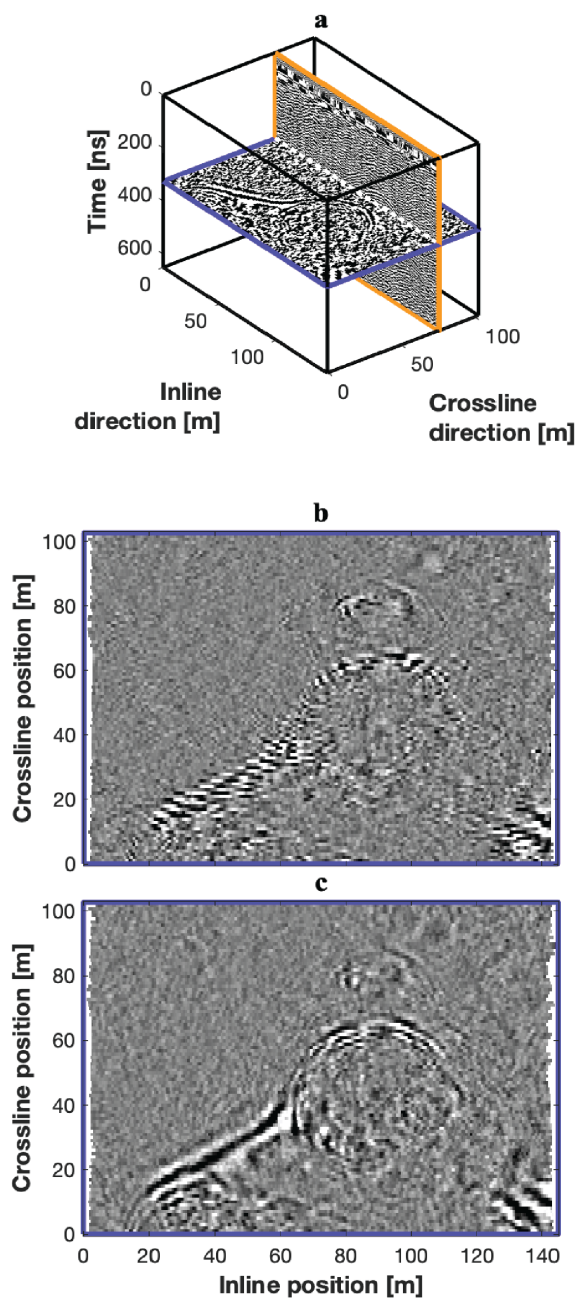
205

Figure 4: Results of applying cross-correlation-based profile shifting to the July 2022 dataset. (a) 3D view of the data volume highlighting the timeslice at 325 ns (purple) displayed in (b) and (c), as well as the inline profile at a crossline position of 76 m (orange) displayed in Fig. 5. (b) and (c): Timeslice at 325 ns before and after application of the shifting, respectively.
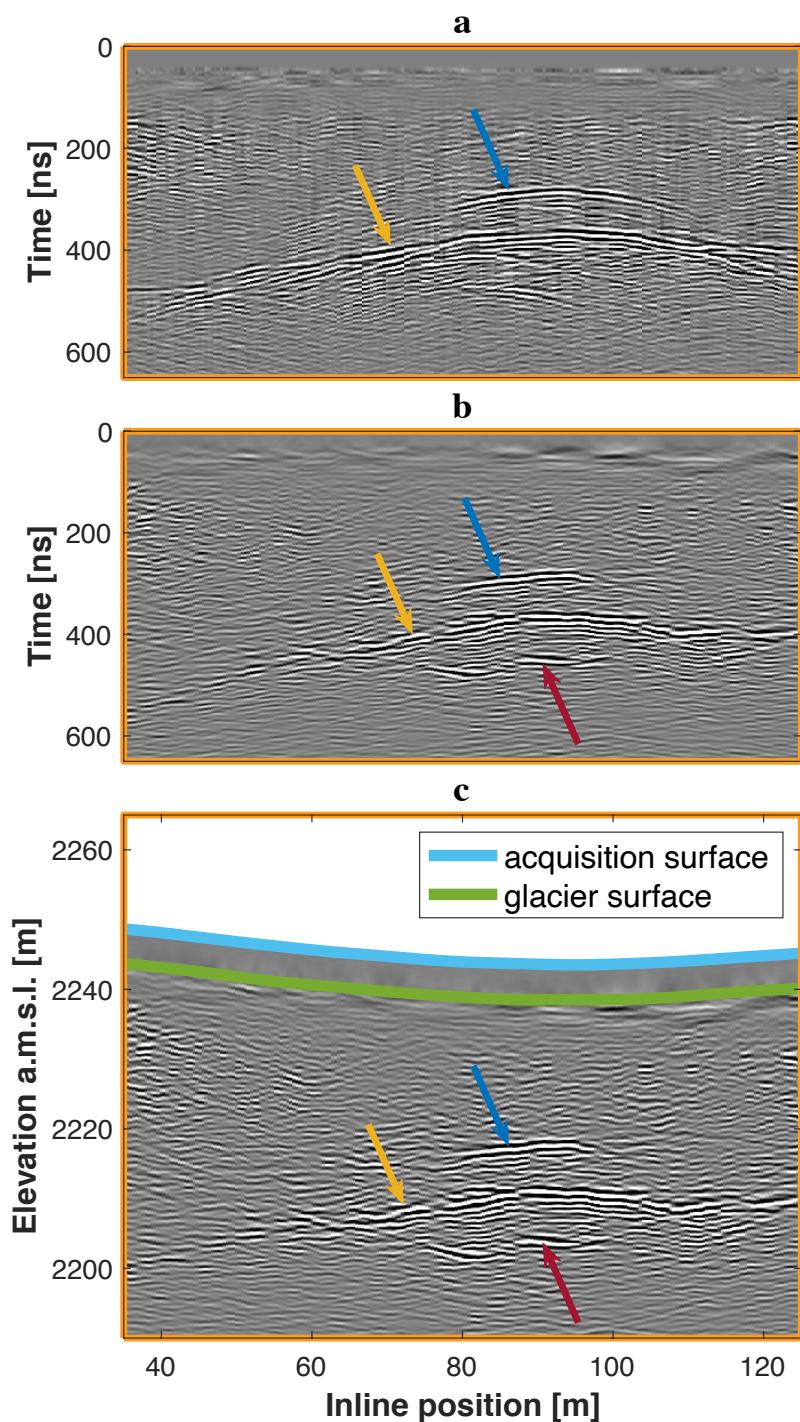
Figure 5: Results of applying 3D migration to the July 2022 dataset, showing part of the inline profile at a crossline position of 76 m (Fig. 4a) (a) in time before migration, (b) in time after migration, and (c) in depth after migration. Blue, yellow, and red arrows point to the roof of the air cavity, the bedrock interface, and a multiple reflection from the bedrock interface, respectively.

210
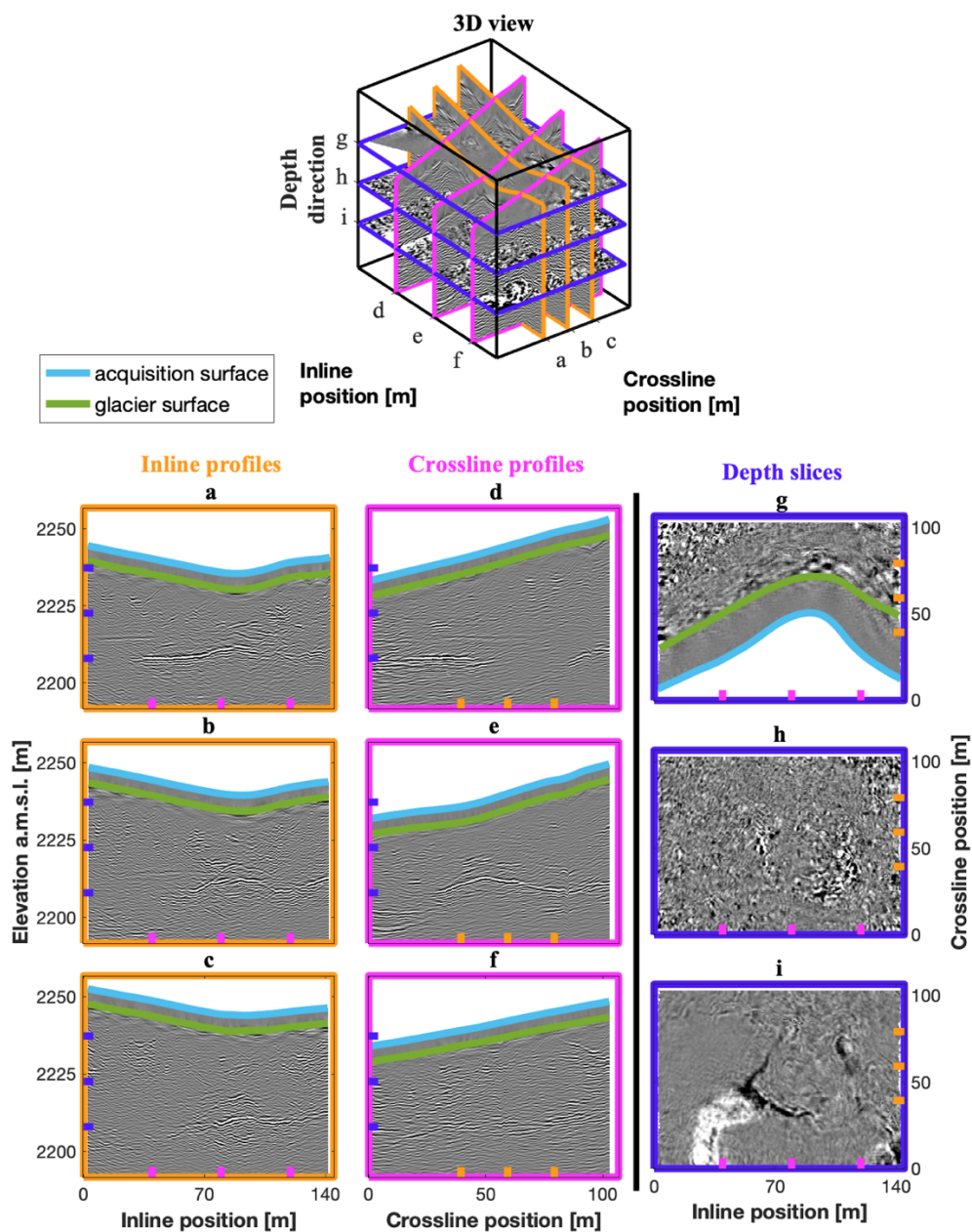
Figure 6: 3D visualization of the July 2022 dataset. The 3D view (up) shows the location of the three selected inline profiles (orange), crossline profiles (pink), and depth slices (purple) displayed on the bottom. (a) to (c): Inline profiles at crossline positions of 39 m, 59 m, and 79 m, respectively. (d) to (f): Crossline profiles at inline positions of 40 m, 80 m, and 120 m, respectively. (g) to (i): Depth slices at 2238 m, 2224 m, and 2208 m a.m.s.l., respectively.

3.5 Bedrock surface and amplitude analysis

220   A commonly used technique to identify the position of subglacial channels in 3D GPR data is to analyze the amplitude characteristics of the reflection near the glacier bed (Egli et al., 2021a; Church et al., 2021). Indeed, because of the stronger contrast in dielectric permittivity between ice and water or air than between ice and bedrock, subglacial channels are expected to be associated with higher GPR reflection amplitudes (e.g., Wilson et al., 2014; Church et al., 2019; Egli et al., 2021a). To this end, we first construct a 3D model of the bedrock reflection surface for each dataset and examine the GPR

225   amplitudes. Bedrock picking is performed manually on the inline profiles (Fig. 7a), the results of which are verified on both the crossline profiles and depth slices, with visible inconsistencies being removed. Next, we fit a preliminary smooth surface (local linear regression) to these picks (Fig. 7b). After removing obvious outliers, a new surface is fitted to the picks to yield the final estimate of the bedrock (Fig. 7c). One item that arises is a circular rise in the bedrock surface at the location of the collapse feature. This is an artifact that results from the assumption of a constant radar wave speed in the glacier ice when

230   migrating the GPR data, when in fact an air-filled cavity exists at this location. Note, however, that this bedrock "pull-up" artifact does not impact our amplitude analysis introduced in the following sentences.

To extract amplitude information along the glacier bed, we follow Egli et al. (2021a) and apply a linear Fourier phase shift to each trace to flatten the data along the estimated bedrock surface, which is followed by calculation of the instantaneous amplitude attribute using the Hilbert transform (e.g., Taner et al., 1979; Chopra and Marfurt, 2007). To

235   compensate for any errors in the estimated bedrock location, the maximum reflection strength is computed for each individual trace over a vertical 2-m window containing the bed reflection (Egli et al., 2021a). Traces located less than 5 m from the border of the GPR grid are not considered to avoid boundary effects related to suboptimal 3D migration. The results of the bedrock reflection amplitude analysis for the four GPR acquisitions, superimposed over the corresponding DOP, are displayed in Fig. 8.

240
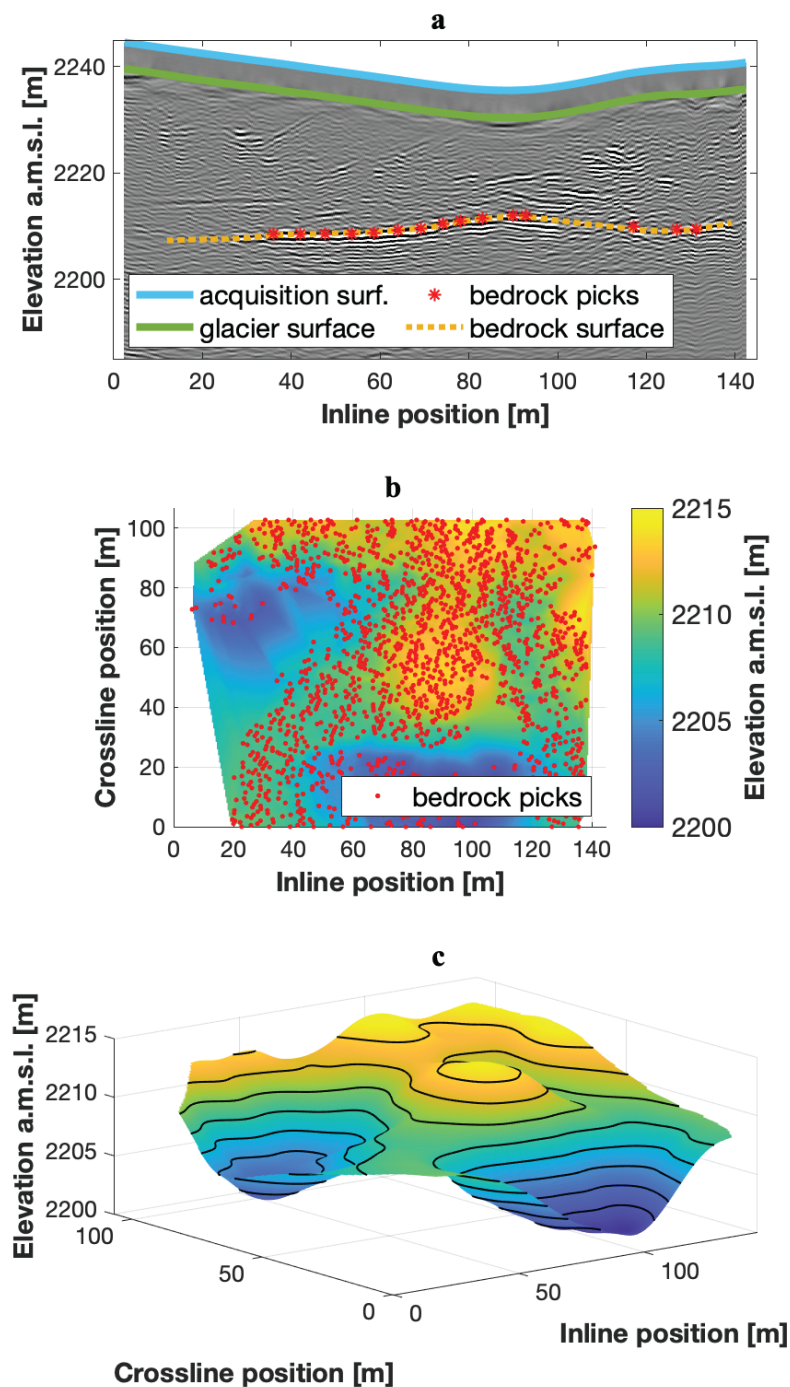
Figure 7: 3D model of the bedrock interface for the July 2022 dataset. (a) Example inline profile from Fig. 6a with bedrock pick locations (red) and smoothed surface (yellow). (b) Locations of the picks for the whole dataset, plotted over the preliminary smoothed bedrock surface. (c) 3D view of the final 3D model of the bedrock surface.
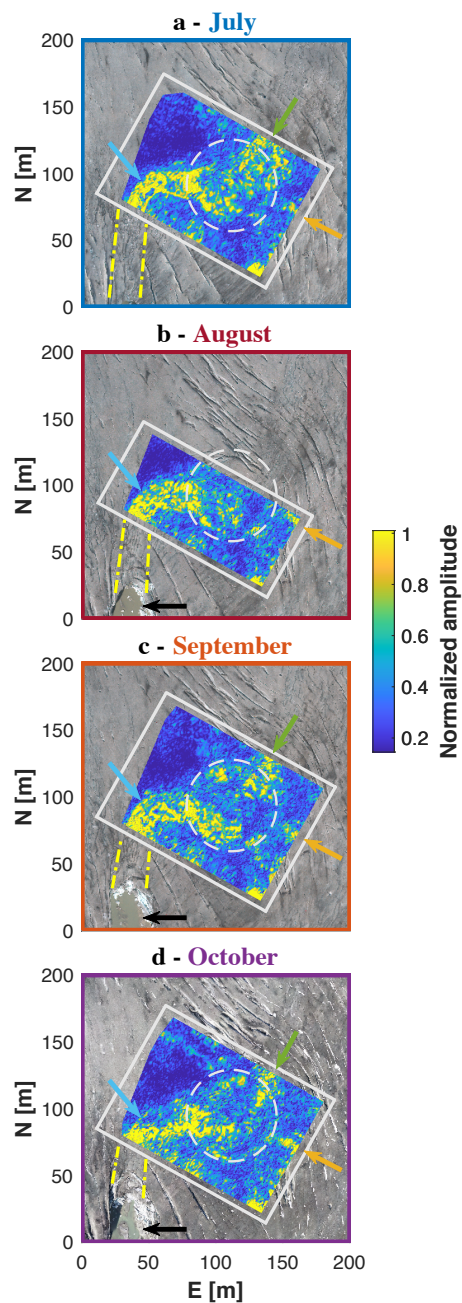
Figure 8: Results of the amplitude analysis at the bedrock interface for the four acquisitions, plotted over the DOP from the same month. The white squares depict the borders of the corresponding GPR dataset. The dashed white circles indicate the approximate location of the circular crevasses. The green and yellow arrows show the potential locations of two subglacial channels entering the collapse feature from the northeast and southeast, respectively (see Fig. 11). The blue arrows indicate the subglacial channel leaving the feature from the west and turning towards the south. The dashed yellow lines highlight the potential connection with the channel outlet (black arrows) visible on the DOP. Northing (N) and Easting (E) are relative to 1159540 m and 2672690 m in the CH1903+ coordinate system, respectively.

250

4. Results

Our amplitude analysis (Fig. 8) reveals the potential locations of two subglacial channels entering the collapse feature, corresponding with regions of higher reflection strength: (i) a main channel entering from the northeast, and (ii) a smaller channel entering from the southeast. Within the collapse feature, the bedrock reflection amplitude is heterogeneous, but the trend of a meander turning from the northeast to the west can be seen. Further down glacier, the suspected subglacial channel leaving the collapse feature from the west appears to turn towards the south in the direction of the channel outlet visible on the background DOP.

To investigate the temporal evolution of the glacier internal structures over the summer of 2022, the processing workflow described in Section 3 was applied to the four GPR acquisitions using common binning parameters. This allowed for the corresponding 3D GPR data volumes to be directly compared. Figure 9 shows the evolution of parts of two selected inline profiles, whose positions are indicated in Fig. 9a. The first profile (Fig. 9b-e) spans the location where the main subglacial channel leaves the collapse feature and shows a distinct internal reflector which we interpret to be the channel roof. This reflector is not yet separable from the bed reflection in the July survey (Fig. 9b), but it becomes apparent in August (Fig. 9c) and evolves over time (Fig. 9d-e). In the October survey (Fig. 9e), a second reflection becomes visible above the subglacial channel, which is possibly related to the appearance of fractures caused by subsidence of the channel roof. The second considered inline GPR profile (Fig. 9f-i) passes through the center of the main collapse feature. Here, a continuous reflector remains visible for all surveys, which we interpret as the roof of the underlying air cavity. Note that at this location, the glacier surface elevation can be seen to decrease throughout the summer. This is a result of both surface ice melt and subsidence, the latter being due to a combination of ice creep into the cavity and partial mechanical failure.

Following the same picking process as for the bedrock reflection (Section 3.5), we tracked the evolution of the air cavity under the Rhône collapse feature over the summer of 2022. Figures 10a-d display the resulting 3D models for the July, August, September, and October acquisitions, respectively, along with the estimated bedrock surface in light grey and the glacier surface in light blue for reference. The minimum thickness of the ice roof above the cavity and the maximum cavity height, as estimated from our results, are summarized in Table 2. Finally, Videos V3 to V14 contain animations showing the full 3D models obtained for the four surveys.

Table 2: Air cavity characteristics from the 4D GPR measurements.

Dataset	Minimum ice roof thickness [m]	Maximum cavity height [m]
July	9.6	15.9
August	6.1	16.8
September	5.3	16.9
October	3.0	18.4
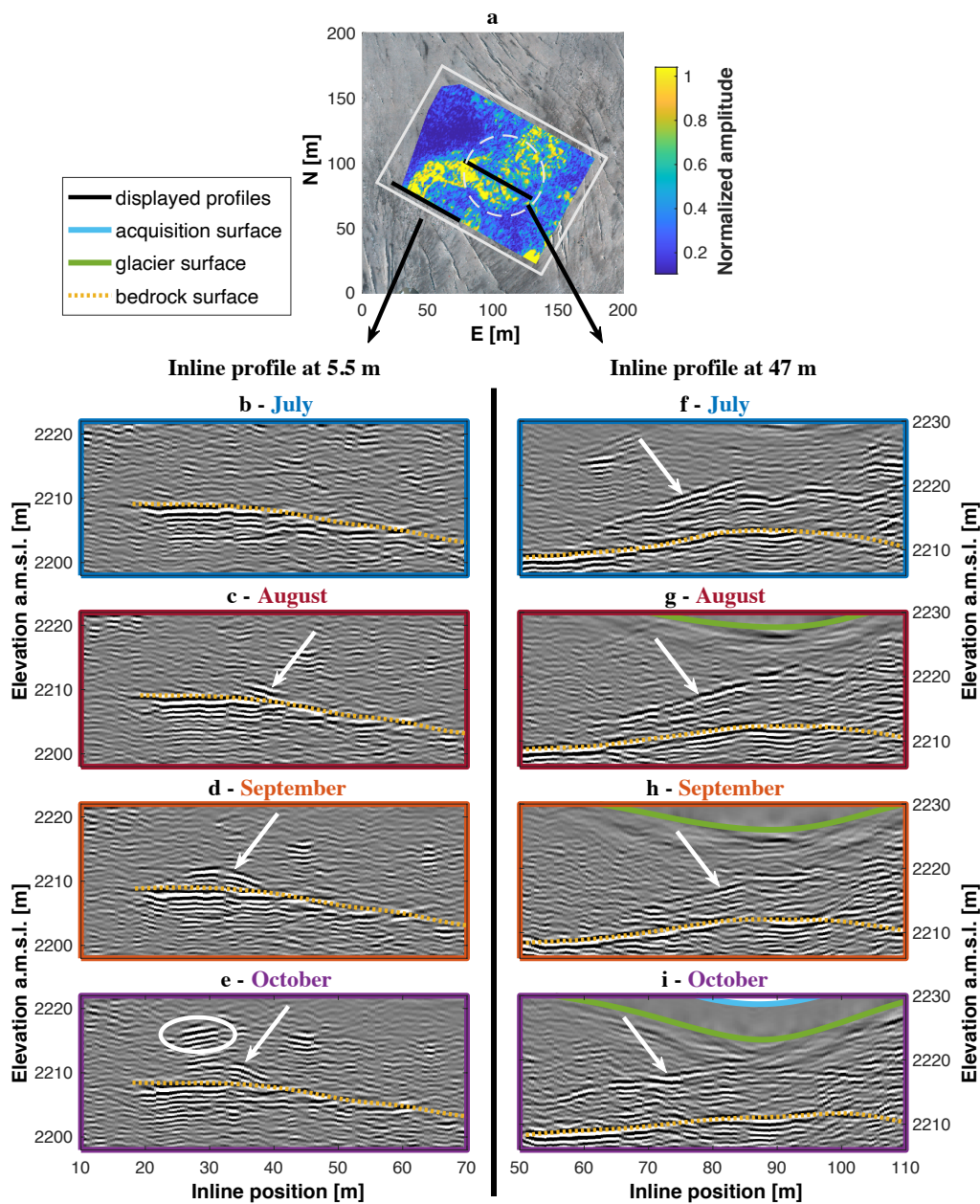
Figure 9: Visualization of the Rhône glacier datasets over the summer of 2022 through a comparison of two inline profiles. (a) Amplitude analysis result for the July dataset, plotted over the DOP from the same month. The white square depicts the border of the GPR grid. The two black lines show the sections of the two selected profiles, located at crossline positions of 5.5 m and 47.0 m. Northing (N) and Easting (E) are relative to 1159540 m and 2672690 m in the CH1903+ coordinate system, respectively. (b) to (e): Inline profiles at 5.5 m, focusing on the channel outlet. The white arrows and circle indicate the channel roof and a large englacial reflection, respectively. (f) to (i): Inline profiles at 47.0 m, focusing on the collapse feature. The white arrows indicate the roof of the underlying air cavity.
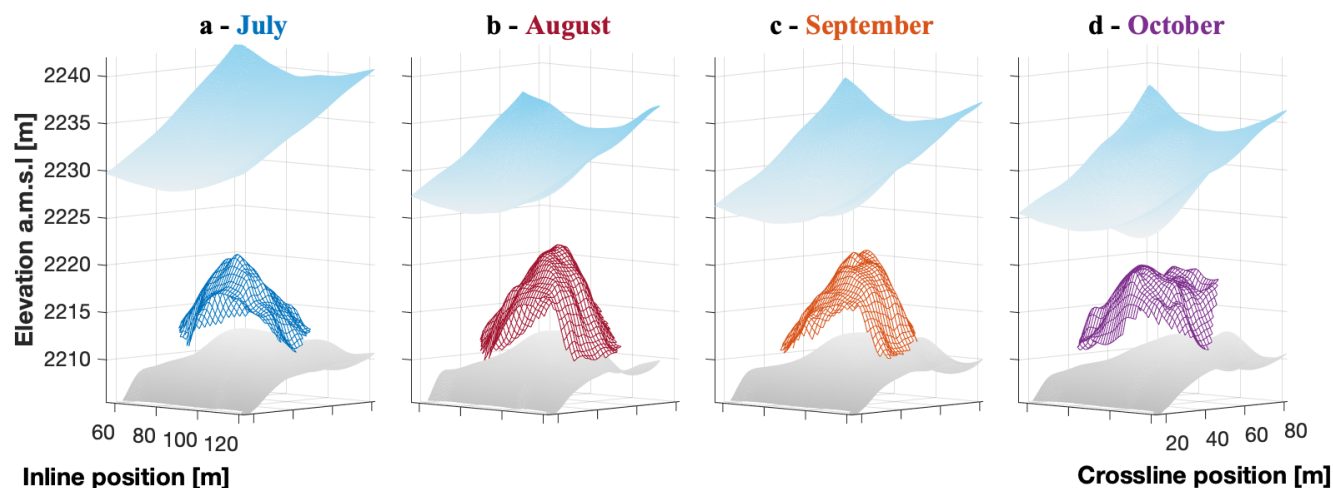
Figure 10: 4D evolution of the collapse feature deduced from the GPR data. (a) to (d) show the 3D models of the underlying air cavity over the summer of 2022, with the bedrock surface plotted in light grey and the glacier surface plotted in light blue for reference.

295

5. Discussion

The results of the amplitude analysis (Fig. 8) suggest that the Rhône collapse feature formed at a peculiar location near the glacier snout where (i) the main subglacial channel forms a meander, and (ii) a secondary channel enters the main channel. Examination of a photograph taken in the summer of 2023 after full collapse of the cavity (Fig. 11) also indicates a localized

300 step (~1 m in height) in the bedrock topography. The combination of these three factors could have led to water turbulence and related energy dissipation, which could ultimately be the process by which the cavity was initiated.

Regarding the two subglacial channels, the main one, originating from the northeast, is likely to drain the majority of the glacier's subglacial water system, whereas the second one, originating from the southeast, likely drains a constrained hydrological basin on the orographic left-hand side of the glacier. Downstream of the collapse feature, a single large

305 subglacial channel is seen to be flowing towards the west and then turning towards the south, i.e. in the direction of Rhône glacier's proglacial lake. Our interpretation of the channel pathways, which is primarily based on our amplitude analysis, was later confirmed by visual observation in September 2023, after the full collapse of the subglacial cavity and the direct exposure of both the bedrock and the glacier's water channels (Fig. 11). We argue that this ground truthing is amongst the most compelling evidence for the potential that lies in the applied methodologies.

310 Further down glacier, the main channel outlet is also seen to be evolving through time (Fig. 8): it has a meandering yet comparatively narrow shape in July, slowly straightens and enlarges during summer, and appears almost straight in October. A distinct reflection from what we interpret as the channel roof appears in August (Fig. 9c) and rises from the bedrock during the course of the summer (Fig. 9d-e). Above this channel roof, further internal reflections appear in October,

which could stem from air-filled fractures that form as ice lamellas start detaching and falling into the channel. Because the imaged part of the channel is located close to the glacier portal, which consists of an ice arch measuring approximately 10 m in height (Fig. 12), the channel is likely unpressurized and air-filled most of the time. In such conditions, warm air can enter the channel from the glacier portal, and we suggest that the heat advected in this way may have contributed to ice melt at the channel walls, thus favoring the fast evolution seen with our 4D imaging.

Finally, the temporal evolution of the main cavity beneath the circular crevasses could be monitored with our 4D survey as well (Fig. 9f-i and Fig. 10). The results show that the thickness of the ice roof decreases while the height of the cavity increases as the collapse feature evolves along the summer (Table 2). The shape of the cavity remains similar between July and September, while it appears to have gained in width in October (Fig. 10). Egli et al. (2021b) suggested that warm air can enter cavities from the glacier front when a widely open and unpressurized channel connects the glacier portal to a cavity. In our case however, the channel between the portal and the cavity does not seem air-filled until August (Fig. 9b-e), i.e. well after the cavity started to grow. This makes air circulation an unlikely driving mechanism up to that stage. After August, when the subglacial channel seems air-filled, this process might have played a role and enhanced the air cavity evolution. As an alternative, Räss et al. (2023) hypothesized that the collapse feature at Rhône glacier grew by mechanical failure of ice lamellas and the subsequent melting and transport of the ice by the subglacial stream. This latter hypothesis is supported by Fig. 13, showing two images from inside the air cavity acquired in August 2022. Large blocks of ice can be seen resting on the cavity floor, which must have collapsed from the ice roof and are likely to deplete over time through a combination of melt and fluvial transport. The latter observation also explains the heterogeneous results in amplitude analysis at the bedrock interface beneath the collapse feature (Fig. 8). The interplay between the various processes causes the question of which of them might dominate the overall evolution.
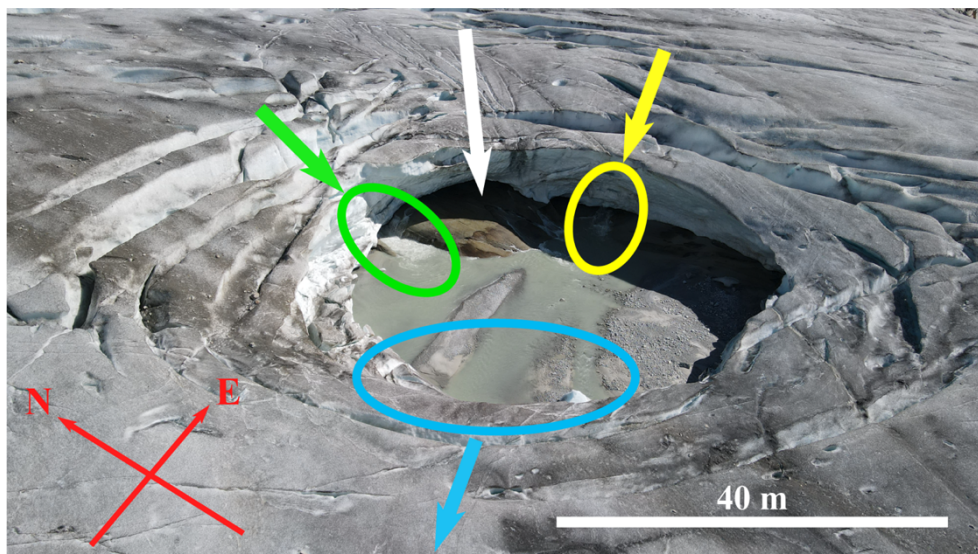
Figure 11: Picture of the studied feature after its full collapse, taken on 11 September 2023. Two water channels entering the feature from the north (green) and east (yellow) are visible, as well as one leaving the feature towards the west (blue). The white arrow points to an observed step (~1 m in height) in the bedrock topography.
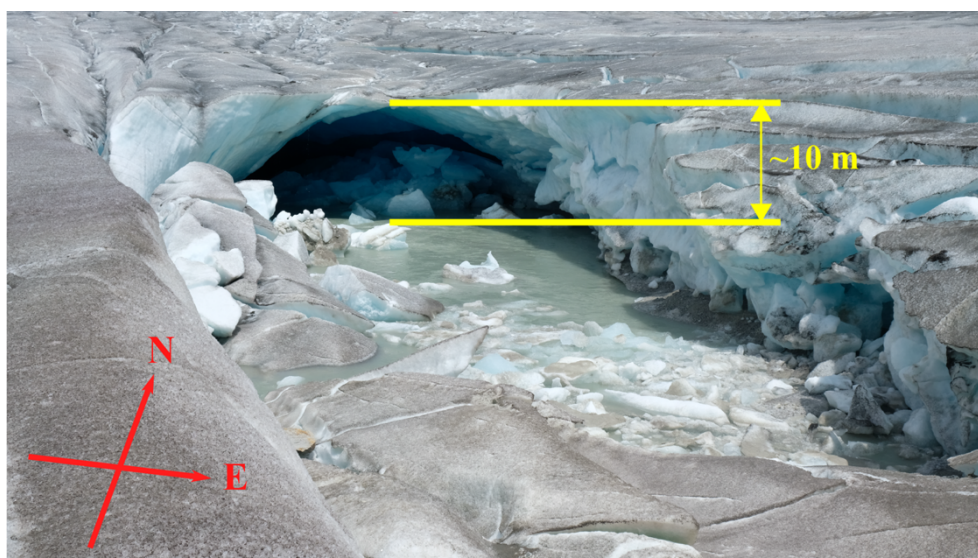
Figure 12: Picture of the channel outlet at the glacier front, taken on 28 July 2022.
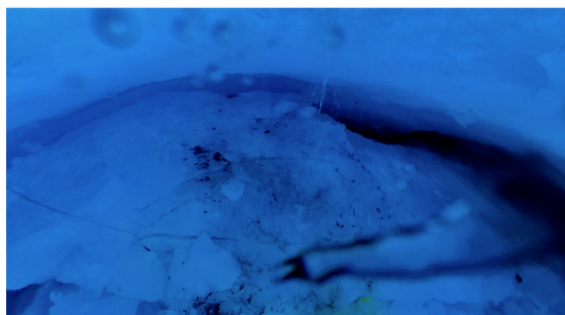
Figure 13: Images taken from a video recorded inside the subglacial cavity by ETH Zürich's VAW Glaciology group. (a) East direction. (b) West direction. Large blocks of ice that have fallen from the ice roof are seen to have accumulated over the bedrock
345   **surface.**

6. Conclusion

In this paper, we have presented a high-density 4D GPR dataset collected over an alpine glacier. It focuses on a surface collapse feature that evolved during the summer of 2022 on the terminal part of Rhône glacier (Switzerland). The GPR data provide detailed insights into the temporal evolution of the glacier's internal structure and allow two main conclusions to be

350   made. The first relates to the genesis of the collapse feature: it initially emerged at a location where the main subglacial water channel meanders and merges with a secondary smaller water channel, and where the bedrock topography displays a small step. After initiation, the subglacial cavity grew by a combination of processes including subglacial ice melt and mechanical failure, with lamellas of ice detaching from the cavity roof. This led to a continuous decrease of the ice roof thickness, favoring further instability. At the surface, these processes resulted in a set of visually concentric circular

355   crevasses, ultimately resulting in the mechanical failure of the cavity roof. The second conclusion relates to the temporal evolution of the main subglacial channel downstream of the main cavity. Here, the channel was seen to quickly evolve during summer, both in shape and in size. Since the channel appears to have been unpressurized for most of the summer, we attribute this fast evolution to the advection of warm air from the large portal observed at the glacier front, and to the accelerated melt happening at the channel walls through this advection.

The investigations were made possible by a newly developed drone-based GPR system which allows for the acquisition of high-density 4D GPR data over glaciers. While the surveyed area (approximately 100 m x 150 m) might be considered to be relatively small, our results show strong potential for using repeated, high-resolution GPR surveys in combination with amplitude analysis for investigating the temporal evolution of the subglacial drainage system in detail. We anticipate that the demonstration of these new capabilities will spur a new line of investigations, ultimately resulting in important glaciological advances.

Video supplements. They will be uploaded and doi provided on a dedicated platform as requested in due time after review. For now, they are available at the following url with the password 'collapse_22':

https://unils-my.sharepoint.com/:f:/g/personal/bastien_ruols_unil_ch/Ekwcougm41FCvXsj0LYSn7gBc2dNsUUyrgkGPlkG4CZl3A?e=J8PIuN

- **Video V1: Drone-based GPR system taking off and beginning the data acquisition on 10 October 2022.**
- **Video V2: Drone-based GPR system acquiring data over the circular crevasses on 10 October 2022.**
- **Videos V3-V14: Animations showing the full 3D models obtained for the four surveys.**

Supplementary Material. One .pdf file was uploaded alongside this manuscript.

Author contributions. Bastien Ruols and Johanna Klahold planned and conducted fieldwork together. Bastien Ruols designed the GPR surveys and operated the drone-based GPR system. Daniel Farinotti gave access to the DOPs used in this study. Bastien Ruols processed and interpreted the drone-based GPR data under the supervision of James Irving. Bastien Ruols wrote the manuscript, which was revised by James Irving and Daniel Farinotti. For analysis and discussion, James Irving and Daniel Farinotti provided geophysics and glaciology expertise, respectively. Final version of the manuscript was reviewed by all co-authors.

Competing interests. Some authors are members of the editorial board of journal The Cryosphere.

Acknowledgments. We thank Mélissa Francey, Pascal Egli, Ben Robson, and Alexi Morin for their substantial help with fieldwork on the Rhône glacier. We also acknowledge the Laboratory of Hydraulics, Hydrology and Glaciology (VAW) for synchronizing fieldwork and providing the photogrammetry data. We acknowledge the use of OpenAI's ChatGPT language model for assistance with editing and refining the text of this manuscript (OpenAI, 2024). This work was supported by grant from the Swiss National Science Foundation to J. Irving (grant nr. 200021_188575, UNIL part) and D.Farinotti (grant nr. 200021_212061, ETHZ part).

References

Allroggen, N., Tronicke, J., Delock, M. and Böniger, U.: Topographic migration of 2D and 3D ground-penetrating radar data considering variable velocities. Near Surf. Geophys., 13: 253-259. doi:10.3997/1873-0604.2014037, 2014.

Bartholomaus, T., Anderson, R., and Anderson, S.: Growth and collapse of the distributed subglacial hydrologic system of Kennicott Glacier, Alaska, USA, and its effects on basal motion. J. Glaciol., 57: 985-1002. doi:10.3189/002214311798843269, 2011.

Binder, D., Brückl, E., Roch, K. H., Behm, M., Schöner, W., and Hynek, B.: Determination of total ice volume and ice-thickness distribution of two glaciers in the Hohe Tauern region, Eastern Alps, from GPR data. Ann. Glaciol., 50: 71–79. doi:10.3189/172756409789097522, 2009.

Catapano, I., Gennarelli, G., Ludeno, G., Esposito, G., and Soldovieri, F.: Contactless Ground Penetrating Radar Imaging. IEEE Geosci. Remote S., 10: 251-273. doi:10.1109/MGRS.2021.3082170, 2022.

Chopra, S., Marfurt, K.: Seismic Attributes for Prospect Identification and Reservoir Characterization. Society of Exploration Geophysicists. doi:10.1190/1.9781560801900, 2007.

Church, G., Bauder, A., Grab, M., Hellmann, S., and Maurer, H.: High-resolution helicopter-borne ground penetrating radar survey to determine glacier base topography and the outlook of a proglacial lake. 2018 17th International Conference on Ground Penetrating Radar (GPR), Rapperswil, Switzerland, 1-4. doi:10.1109/ICGPR.2018.8441598, 2018.

Church, G., Bauder, A., Grab, M., Rabenstein, L., Singh, S., and Maurer, H. R.: Detecting and characterising an englacial conduit network within a temperate Swiss glacier using active seismic, ground penetrating radar and borehole analysis. Ann. Glaciol., 60: 193–205. doi:10.1017/aog.2019.19, 2019.

Church, G., Bauder, A., Grab, M., and Maurer, H.: Ground-penetrating radar imaging reveals glacier's drainage network in 3D. The Cryosphere, 15: 3975–3988. doi:10.5194/tc-15-3975-2021, 2021.

Church, G., Grab, M., Schmelzbach, C., Bauder, A., and Maurer, H.: Monitoring the seasonal changes of an englacial conduit network using repeated ground-penetrating radar measurements. The Cryosphere, 14: 3269–3286. doi:10.5194/tc-14-3269-2020, 2020.

Del Gobbo, C., Colucci, R. R., Forte, E., Triglav Čekada, M., and Zorn, M.: The Triglav Glacier (South-Eastern Alps, Slovenia): Volume Estimation, Internal Characterization and 2000–2013 Temporal Evolution by Means of Ground Penetrating Radar Measurements. Pure Appl. Geophys., 173: 2753–2766. doi:10.1007/s00024-016-1348-2, 2016.

Dewald, N., Lewington, E., Livingstone, S., Clark, C., and Storrar, R.: Distribution, characteristics and formation of esker enlargements. Geomorphology, 392. doi:10.1016/j.geomorph.2021.107919, 2021.

Egli, P., Belotti, B., Ouvry, B., Irving, J., and Lane, S.: Subglacial Channels, Climate Warming, and Increasing Frequency of Alpine Glacier Snout Collapse. Geophys. Res. Lett., 48: 1–11. doi:10.1029/2021GL096031, 2021b.

Egli, P., Irving, J., and Lane, S.: Characterization of subglacial marginal channels using 3-D analysis of high-density ground-
425 penetrating radar data. J. Glaciol., 67: 759–772. doi:10.1017/jog.2021.26, 2021a.

Farinotti, D., Huss, M., Bauder, A., Funk, M., and Truffer, M.: A method to estimate the ice volume and ice-thickness distribution of alpine glaciers. J. Glaciol., 55: 422–430. doi:10.3189/002214309788816759, 2009.

GLAMOS: The Swiss Glaciers 2013/14 and 2014/15, Bauder, A. (ed.), Glaciological Report No. 135/136 of the Cryospheric Commission (EKK) of the Swiss Academy of Sciences (SCNAT) published by VAW / ETH Zürich.
430 doi:10.18752/glrep_135-136, 2017.

GLAMOS: The Swiss Glaciers 2019/20 and 2020/21. Bauder, A., Huss, M., Linsbauer, A. (eds), Glaciological Report No. 141/142 of the Cryospheric Commission (EKK) of the Swiss Academy of Sciences (SCNAT) published by VAW / ETH Zürich. doi:10.18752/glrep_141-142, 2022.

Grab, M., Mattea, E., Bauder, A., Huss, M., Rabenstein, L., Hodel, E., Linsbauer, A., Langhammer, L., Schmid, L., Church,
435 G., Hellmann, S., Délèze, K., Schaer, P., Lathion, P., Farinotti, D., and Maurer, H.: Ice thickness distribution of all Swiss glaciers based on extended ground-penetrating radar data and glaciological modeling. J. Glacio., 67: 1074-1092. doi:10.1017/jog.2021.55, 2021.

Hösli, L., Ogier, C., Huss, M., and Farinotti, D.: Recent increase in collapse features on glacier snouts throughout the Swiss Alps, Swiss Geoscience Meeting 2022, P.15.5. https://geoscience-meeting.ch/sgm2022/wp-
440 content/uploads/abstract_books/SGM_2022_Symposium_15.pdf, 2022.

Irvine-Fynn, T., Moorman, B., Williams, J., and Walter, F.: Seasonal changes in ground-penetrating radar signature observed at a polythermal glacier, Bylots Island, Canada. Earth Surf. Proc. Land., 31: 892–909. doi:10.1002/esp.1299, 2006.

Jenssen, R., Eckerstorfer, M., and Jacobsen, S.: Drone-mounted ultrawideband radar for retrieval of snowpack properties. IEEE T. Instrum. Meas., 69: 221–230. doi:10.1109/TIM.2019.2893043, 2020.

445 Kellerer-Pirklbauer A., and Kulmer B.: The evolution of brittle and ductile structures at the surface of a partly debris-covered, rapidly thinning and slowly moving glacier in 1998–2012 (Pasterze Glacier, Austria), Earth Surf. Proc. Land., 44: 1034–1049. doi:10.1002/esp.4552, 2019.

Konrad, S.: Possible outburst floods from debris-covered glaciers in the sierra nevada, California. Geogr. Ann. A., 80: 183-192. doi:10.1111/j.0435-3676.1998.00036.x, 1998.

450 Langhammer, L., Grab, M., Bauder, A., and Maurer, H. R.: Glacier thickness estimations of alpine glaciers using data and modeling constraints. The Cryosphere, 13: 2189–2202. doi:10.5194/tc-13-2189-2019, 2019.

Langhammer, L., Rabenstein, L., Bauder, A., and Maurer, H.: Ground-penetrating radar antenna orientation effects on temperate mountain glaciers. Geophysics, 82: 15–24. doi:10.1190/GEO2016-0341.1, 2017.

455 Langhammer, L., Rabenstein, L., Schmid, L., Bauder, A., Grab, M., Schaer, P., and Maurer, H.: Glacier bed surveying with helicopter-borne dual-polarization ground-penetrating radar. J. Glaciol., 65: 123–135. doi:10.1017/jog.2018.99, 2018.

Lindström, E.: Esker enlargements in northern Sweden. Geogr. Ann. A., 75: 95-110. https://www.jstor.org/stable/521028, 1993.

Murray, T. and Booth, A.: Imaging glacial sediment inclusions in 3-D using ground-penetrating radar at Kongsvegen, Svalbard. J. Quaternary Sci., 25: 754–761. doi:10.1002/jqs.1351, 2010.

460 Ogier, C., Hösli, C., Räss, L., Huss, M., Bauder, A., and Farinotti, D.: Characterization of a glacier collapse feature development at Rhonegletscher, Switzerland. Swiss Geoscience Meeting 2022, P.15.5. https://geoscience-meeting.ch/sgm2022/wp-content/uploads/abstract_books/SGM_2022_Symposium_15.pdf, 2022.

OpenAI: ChatGPT (Version GPT-4). https://openai.com/chatgpt, 2024.

Räss, L., Ogier, C., Utkin, I., Werder, M., Bauder, A., and Farinotti, D.: Mechanical failure to drive the glacier collapse
465 feature at Rhonegletscher, Switzerland, EGU General Assembly 2023, Vienna, Austria, EGU23-9021, doi:10.5194/egusphere-egu23-9021, 2023.

Reinardy, B., Booth, A., Hughes, A., Boston, C., Åkesson, H., Bakke, J., Nesje, A., Giesen, R., and Pearce, D.: Pervasive cold ice within a temperate glacier – implications for glacier thermal regimes, sediment transport and foreland geomorphology, The Cryosphere, 13: 827–843, doi:10.5194/tc-13-827-2019, 2019.

470 Ruols, B., Baron, L., and Irving, J.: Development of a drone-based groundpenetrating radar system for efficient and safe 3D and 4D surveying of alpine glaciers. J. Glaciol., 1–12. doi:10.1017/jog.2023.83, 2023.

Rutishauser, A., Maurer, H. R., and Bauder, A.: Helicopter-borne ground-penetrating radar investigations on temperate alpine glaciers: A comparison of different systems and their abilities for bedrock mapping. Geophysics, 81: 119-129. doi:10.1190/GEO2015-0144.1, 2016.

475 Saintenoy, A., Friedt, J.-M., Tolle, F., Bernard, E., Laffly, D., Marlin, C., and Griselin, M.: High density coverage investigation of the Austre LovénBreen (Svalbard) using Ground Penetrating Radar. 2011 6th International Workshop on Advanced Ground Penetrating Radar, 11–14. doi:10.1109/IWAGPR.2011.5963894, 2011.

Saintenoy, A., Friedt, J.-M., Booth, A., Tolle, F., Bernard, E., Laffly, D., Marlin, C., and Griselin, M.: Deriving ice thickness, glacier volume and bedrock morphology of Austre Lovénbreen (Svalbard) using GPR. Near Surf. Geophys., 11:
480 253–261. doi:10.3997/1873-0604.2012040, 2013.

Schroeder, D.: Paths forward in radioglaciology. Ann. Glaciol., 63: 13-17. https://doi.org/10.1017/aog.2023.3, 2022.

Schroeder, D., Bingham, R., Blankenship, D., Christianson, K., Eisen, E., Flowers, G., Karlsson, N., Koutnik, M., Paden, J., and Siegert, M.: Five decades of radioglaciology. Ann. Glaciol., 61: 1–13. doi:10.1017/aog.2020.11, 2020.

Stocker-Waldhuber, M., Fischer, A., Keller, L., Morche, D., and Kuhn, M.: Funnel-shaped surface depressions — Indicator or accelerant of rapid glacier disintegration? A case study in the Tyrolean Alps, Geomorphology, 287: 58-72, doi:10.1016/j.geomorph.2016.11.006, 2017.

Swisstopo. Map of Switzerland. Federal Office of Topography. Accessed in April 2024. https://map.geo.admin.ch, 2024.

Tan, A., McCulloch, J., Rack, W., Platt, I. and Woodhead, I.: Radar Measurements of Snow Depth Over Sea Ice on an Unmanned Aerial Vehicle. *IEEE T. Geosci. Remote*, 59: 1868-1875, doi:10.1109/TGRS.2020.3006182, 2021.

Taner, M., Koehler, F., and Sheriff, R.: Complex seismic trace analysis. Geophysics, 44: 1041-1063. doi:10.1190/1.1440994, 1979.

Tsutaki, S., Sugiyama, S., Nishimura, D., and Funk, M.: Acceleration and flotation of a glacier terminus during formation of a proglacial lake in Rhonegletscher, Switzerland. J. Glaciol., 59: 559-570. doi:10.3189/2013JoG12J107, 2023.

Valence, E., Baraer, M., Rosa, E., Barbecot, F., and Monty, C.: Drone-based ground-penetrating radar (GPR) application to snow hydrology. The Cryosphere, 16: 3843–3860. doi:10.5194/tc-16-3843-2022, 2022.

Wilson, N., Flowers, G., and Mingo, L.: Mapping and interpretation of bed-reflection power from a surge-type polythermal glacier, Yukon, Canada. Ann. Glaciol., 55: 1-8. doi:10.3189/2014AoG67A101, 2014.

Woodward, J., and Burke, B.: Applications of Ground-Penetrating Radar to Glacial and Frozen Materials. J Environ. End. Geoph., 12: 69-85. doi:10.2113/JEEG12.1.69, 2007.